

Engineering biphoton spectral wavefunction in a silicon micro-ring resonator with split resonances

Liao Ye,¹ Haoran Ma,¹ Xiaoqing Guo,¹ Fanjie Ruan,¹
Yuehai Wang,¹ and Jianyi Yang^{1,*}

Institute of Microelectronic and Nanoelectronics,
College of Information Science and Electronics Engineering,
Zhejiang University, Hangzhou 310027, China
12031018@zju.edu.cn

August 27, 2024

Abstract

Frequency-time is a degree of freedom suitable for photonic high-dimensional entanglement, with advantages such as compatibility with single-mode devices and insensitivity to dispersion. The engineering control of the frequency-time amplitude of a photon's electric field has been demonstrated on platforms with second-order optical nonlinearity. For integrated photonic platforms with only third-order optical nonlinearity, the engineered generation of the state remains unexplored. Here, we demonstrate a cavity-enhanced photon-pair source on the silicon-on-insulator (SOI) platform that can generate both separable states and controllable entangled states in the frequency domain without post-manipulation. By choosing different resonance combinations and employing on-chip optical field differentiation, we achieve independent control over two functions that affect the joint spectral intensity (JSI) of the state. A semi-analytical model is derived to simulate the biphoton spectral wavefunction in the presence of resonance splitting and pump differentiation, and its parameters can be fully determined through fitting-based parameter extraction from the resonator's measured linear response. The measured spectral purity for the separable state is $95.5 \pm 1.2\%$, while the measured JSIs for the entangled states show two- or four-peaked functions in two-dimensional frequency space. The experiments and simulations demonstrate the capacity to manipulate the frequency-domain wavefunction in a silicon-based device, which is promising for applications like quantum information processing using pulsed temporal-mode encoding or long-distance quantum key distribution.

1 Introduction

Recent advances in quantum photonic systems using photonic integrated circuits (PICs) have demonstrated excellent stability, scalability, and programmability [1–3], enabling the efficient generation and manipulation of multiphoton [4, 5] or high-dimensional [2, 3, 6–9] quantum states on a single chip. High-dimensional entangled states, in particular, have received much attention due to their versatile applications and significant advantages. They enhance quantum computation efficiency [3, 10] and exhibit noise-resistant and dense-encoding capabilities in quantum communications [11–13]. In recent years, photonic entangled states based on different degrees of freedom (d.o.f.s), such as path [2,3,6], frequency-time [7–9,14], and transverse spatial modes [15], have been proposed and experimentally demonstrated on PICs.

Frequency-time, as a potential on-chip d.o.f., enables the encoding of quantum information in high-dimensional Hilbert spaces within specific spatial structures, such as single-mode photonic integrated devices [16] and single-mode optical fibers. Many recent on-chip frequency-time schemes concentrate on creating and manipulating frequency-bin [7–9] or time-bin [14] states. However, due to the discrete nature of bins, these states have a finite number of encodable dimensions within specific frequency or time ranges. Another potential method is to encode quantum information in the complex frequency-time amplitude of a single photon's electric field [17], which theoretically offers arbitrary encodable dimensions within a specific frequency range [16] and could reach the continuous variable (CV) quantum information regime at high dimensionality [18–21]. The controlled generation of these states has been extensively demonstrated using parametric down-conversion (PDC) on various second-

order optical nonlinear platforms [18, 21–25]. To our knowledge, no experiment has yet demonstrated the controlled generation of such frequency-time states on third-order optical nonlinear platforms, such as silicon-on-insulator (SOI). Adapting this scheme to the SOI platform offers significant advantages, including the use of well-developed photonic arbitrary waveform generating [26, 27] or signal processing [28] devices to engineer the spectral or temporal amplitude and phase of pump pulses. This allows for direct shaping of biphoton joint spectral amplitude (JSA) at the generation stage, avoiding post-manipulation that reduces the source’s brightness [21, 23] or the use of 4-f pulse shapers [21–23, 29], which weakens integrability.

In single-mode silicon waveguides, the interacting optical fields in spontaneous four-wave mixing (SFWM) have wavelengths that differ by only a few to several tens of nanometers [30, 31], and their velocities satisfy the symmetric group velocity matching (sGVM) condition [16]. This results in broad phase-matching bands near the pump wavelength [32]. However, the controlled generation of biphoton entangled or separable states needs a joint spectral distribution in narrow frequency ranges for both signal and idler photons, as demonstrated in the schemes based on the type-II PDC process [18, 21–23]. Thus, it is necessary to introduce additional devices, such as micro-ring resonators (MRRs), to implement direct filtering to constrain broadband phase-matching at the generation stage, as well as to achieve high source brightness due to their field enhancement. MRRs have preliminarily been used as heralded single-photon sources with high spectral purity [31–33]. In addition, while resonance splitting is employed to regulate the field enhancement function of MRRs, its impact on the spectral wavefunction of photon pairs has only been theoretically investigated [34] and not experimentally validated.

In this work, we demonstrate a cavity-enhanced photon-pair source on the SOI platform that exhibits flexibility in engineering biphoton spectral wavefunctions without post-manipulation. The device is based on an all-pass MRR with split resonances due to backscattering. The experiment begins with the generation of a nearly separable biphoton state in the frequency domain, followed by the sequential adjustment of the predefined two-dimensional signal-idler (TDSI) and antidiagonal pump (ADP) functions to generate two types of biphoton entangled states, respectively. The TDSI function is controlled by adjusting the pump’s central wavelength to choose different resonance combinations, while the ADP function is controlled by on-chip differentiation of the pump field (via another MRR-based optical temporal differentiator). Additionally, the biphoton spectral wavefunction for

SFWM in the presence of intra-cavity backward propagating modes, as well as analytical expressions for the TDSI and ADP functions, are derived using temporal coupled-mode theory (TCMT). The parameters characterizing the forward and backward propagating modes for specific resonances are obtained from the measured spectra using the fitting method, ensuring the accuracy and reliability of the simulations. The experiments and simulations demonstrate a general method for frequency state preparation on integrated photonic platforms with only third-order optical nonlinearity.

2 Theoretical Framework

2.1 Adjustment of Biphoton Spectral Wavefunction with Split Resonances

Using a standard perturbative approach and neglecting multipair generation, the quantum state generated by the SFWM process in a waveguide with third-order optical nonlinearity can be expressed as [35]

$$|\psi\rangle = |0\rangle_s |0\rangle_i + \beta \iint d\omega_s d\omega_i F(\omega_s, \omega_i) \hat{a}_s^\dagger(\omega_s) \hat{a}_i^\dagger(\omega_i) |0\rangle_s |0\rangle_i, \quad (1)$$

where β represents waveguide length, the material’s third-order nonlinear coefficient, and the pump’s amplitude. ω_s and ω_i are the angular frequencies of signal and idler photons, respectively. The JSA function $F(\omega_s, \omega_i)$ describes the spectral entanglement characteristics of the signal-idler pairs. For a MRR-based photon source driven by a degenerate pulsed pump with a central frequency ω_p , $F(\omega_s, \omega_i)$ is given by the following equation, considering the energy conservation constraint [36, 37]:

$$F(\omega_s, \omega_i) = \int d\omega_p \alpha_p(\omega_p) l_p(\omega_p) \alpha_p(\omega_s + \omega_i - \omega_p) \times l_p(\omega_s + \omega_i - \omega_p) \phi_{PM}(\omega_p, \omega_s, \omega_i) l_s(\omega_s) l_i(\omega_i). \quad (2)$$

Here, $\alpha_p(\omega)$ is the spectral envelope of the degenerate pump, and $l_x(\omega)$ is the ratio of intra-cavity fields to input fields (where $x = p, s, i$), also known as field enhancement. The phase-matching function $\phi_{PM}(\omega_p, \omega_s, \omega_i)$ is determined by the group velocities of the interacting fields under the linear approximation (see Appendix A). For resonances without splitting, $l_x(\omega)$ can be expressed as $l_x(\omega) = \kappa_x / [i(\omega - \omega_x) + 1/\tau_x]$ [38], where κ_x is the field coupling coefficient, ω_x is the resonant frequency, and $1/\tau_x$ is the amplitude decay rate of the intra-cavity field. Considering the resonance splitting occurring in MRR with a high quality factor [39, 40], l_x is altered to l_{xf} and l_{xb} to distinguish between forward and backward propagating modes [34]. The TCMT-derived model (see

Appendix B) describes l_{xf} and l_{xb} as

$$l_{xf}(\omega) = \kappa_x \frac{-\gamma_x \mu_{x,12} + (\omega - \omega_x) - i/\tau_x}{[i(\omega - \omega_x) + 1/\tau_x]^2 + \mu_{x,12} \mu_{x,21}}, \quad (3)$$

$$l_{xb}(\omega) = \kappa_x \frac{-\mu_{x,21} + \gamma_x (\omega - \omega_x) - i\gamma_x/\tau_x}{[i(\omega - \omega_x) + 1/\tau_x]^2 + \mu_{x,12} \mu_{x,21}}, \quad (4)$$

where κ_x is modified to the forward field-coupling coefficient, and γ_x is the ratio of the backward and forward field coupling coefficients in the coupler. $\mu_{x,12}$ and $\mu_{x,21}$ are mutual power coupling coefficients within the ring waveguide, similar to the parameters in Ref. [40]. When resonance splitting is considered, the JSA observed from the output port (forward propagating mode of the bus waveguide) is regarded as the weighted coherent sum of the contributions from four intra-cavity propagating mode pairs of pump-signal/idler resonances [34], including forward-forward (f-f), forward-backward (f-b), backward-forward (b-f), and backward-backward (b-b) pairs. We use the uppercase symbols L and Γ to represent scalar arrays containing these contributions and their weights, respectively. By substituting Eqs. (3) and (4) into Eq. (2) and traversing the forward and backward propagating modes of the pump and signal-idler, we obtain

$$F(\omega_s, \omega_i) = \sqrt{N} \int d\omega_p \alpha_p(\omega_p) \alpha_p(\omega_s + \omega_i - \omega_p) \times \phi_{PM}(\omega_p, \omega_s, \omega_i) \Gamma L, \quad (5)$$

where $\Gamma = (1, \gamma_s \gamma_i, \gamma_p^2, \gamma_p^2 \gamma_s \gamma_i)$, $L = (l_{pf} l_{pf}^{ec} l_{sf} l_{if}, l_{pf} l_{pf}^{ec} l_{sb} l_{ib}, l_{pb} l_{pb}^{ec} l_{sf} l_{if}, l_{pb} l_{pb}^{ec} l_{sb} l_{ib})^T$. \sqrt{N} is the normalization prefactor. l_{pf}^{ec} and l_{pb}^{ec} are the field enhancement terms considering the energy conservation constraint.

2.2 Biphoton Spectral Wavefunction Engineering

In order to improve the reliability of simulations, parameters in Eqs. (3) and (4) for all resonances are determined by fitting the measured transmission spectra (representing the MRR's linear response) to the through-port optical field expression (refer to Appendix B) using a least-squares algorithm. Figure 1 illustrates the fundamental concept of manipulating the biphoton spectral wavefunction in the SFWM process. From Eq. (5), we derive two functions that characterize the distribution of $F(\omega_s, \omega_i)$ in $\{\omega_s, \omega_i\}$ space: the ADP function and the TDSI function, which can be expressed as follows:

$$ADP(\omega_p) = [\alpha_p(\omega_p) l_{pf}(\omega_p)] * [\alpha_p(\omega_p) l_{pf}(\omega_p)] + \gamma_p^2 [\alpha_p(\omega_p) l_{pb}(\omega_p)] * [\alpha_p(\omega_p) l_{pb}(\omega_p)], \quad (6)$$

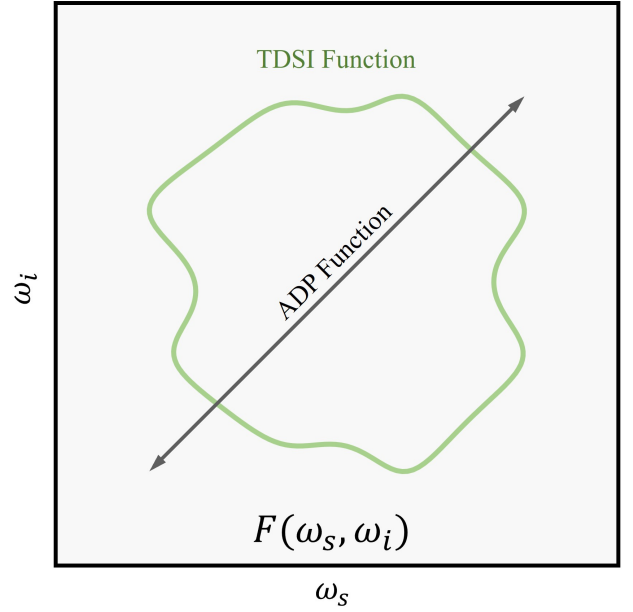


Figure 1: Schematic diagram of the biphoton spectral wavefunction engineering principle.

$$TDSI(\omega_s, \omega_i) = l_{sf}(\omega_s) l_{if}(\omega_i) + \gamma_s \gamma_i l_{sb}(\omega_s) l_{ib}(\omega_i). \quad (7)$$

The ADP function depends on the field enhancement of the pump resonance and the spectrum of the pump pulse, which affects the amplitude and phase spectral distribution of $F(\omega_s, \omega_i)$ along the anti-diagonal direction. The TDSI function is determined by the field enhancement of the signal-idler resonances and serves as a two-dimensional filtering function in $\{\omega_s, \omega_i\}$ space. When resonance splitting occurs, both functions can be expressed as weighted sums of contributions from forward and backward propagating modes, as presented in Eqs. (6) and (7). It is important to emphasize that these two functions can be independently adjusted in experiments. The device is capable of generating nearly separable states when the ADP function is spectrally broadened through pump resonance splitting, as well as controllable entangled states when the TDSI or ADP function is shaped into specific patterns via signal-idler resonance splitting or pump pulse differentiation. The generation of both states and the corresponding engineering methods are demonstrated through simulations and experiments.

3 Device configuration

A MRR-based photonic temporal differentiator has been demonstrated to perform differentiation operations on optical pulses, producing first- or fractional-order differentiated waveforms [41]. Figure 2(f) shows the schematic configuration of our device, comprising two MRRs indirectly coupled through a single-

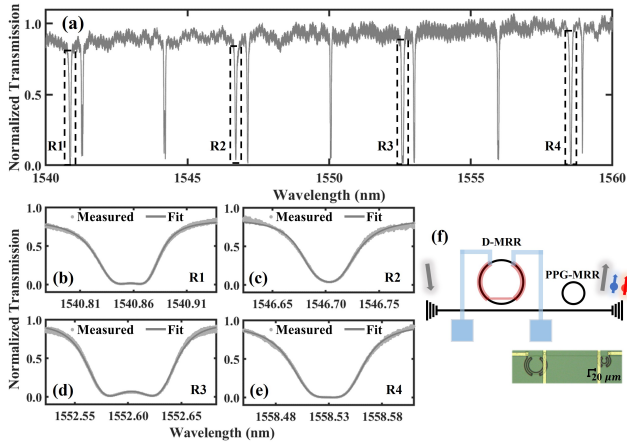


Figure 2: Device configurations. (a) Measured spectrum with a 8 volts heater voltage applied to the D-MRR. (b)-(e) Zoomed-in spectra with their fitted curves of R1 (b), R2 (c), R3 (d), and R4 (e). (f) Schematic configuration of the device. Inset: micrograph of the device.

mode waveguide (450nm \times 220nm cross-section, TE0 mode): one for optical differentiation (D-MRR) and the other for photon-pair generation (PPG-MRR). Both MRRs operate in the over-coupling regime, with D-MRR and PPG-MRR having radii of 30 μ m and 15 μ m, respectively. This results in a free spectral range (FSR) ratio of 1 : 2 and a full width at half maximum (FWHM) ratio of approximately 2 : 5. A TiN heater is fabricated over D-MRR to tune its resonant wavelengths, enabling the pump's differentiation operation to be switched on or off.

We commence with the regime of generating photons with high spectral purity, which means that the JSA of the generated signal-idler photon pairs is separable. This requires setting the heater voltage to 8 volts, thereby separating the resonances of the two MRRs and deactivating the differentiation operation. Figure 2(a) shows the device's spectrum spanning 1540 nm and 1560 nm, with PPG-MRR exhibiting four resonances labeled "R1" through "R4". These are further detailed in Figs. 2(b)-2(e), illustrating varying degrees of resonance splitting. The free parameters in Eqs. (3) and (4) for R1-R4 are determined via fitting and listed in Table 1 (see Appendix B). To achieve high spectral purity in photon generation, the initial experimental setup selects split R3 as the pump resonance, with relatively unsplit R2 and R4 chosen as the signal and idler resonances, respectively, following the pump-split regime described in Ref. [34]. When referring to the regime of entangled state generation, adjustments in heater voltage and resonance combination are necessary.

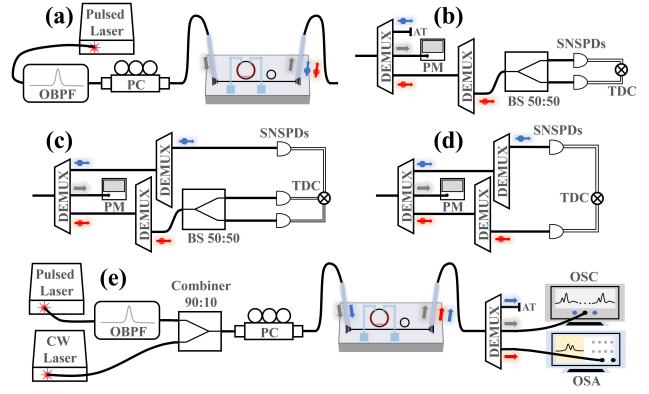


Figure 3: Experimental setups. (a) Sketch of the input setup for (b), (c), and (d). OBPF: optical band-pass filter; PC: polarization controller. (b)-(d) Sketches of the output setups for the unheralded second-order correlation (b), conditioned second-order correlation (c), and brightness (d) experiments. DEMUX: demultiplexer; AT: absorbing termination; PM: power meter; BS: beam splitter; SNSPD: superconducting nanowire single-photon detector; TDC: time-to-digital converter. (e) Sketch of the stimulated emission tomography experiment. OSC: oscilloscope; OSA: optical spectrum analyzer.

4 Experimental setup

The experimental setup is shown in Figs. 3(a)-3(e). Pump pulses are generated by a pulsed erbium-doped fiber laser (Pritel, tunable central wavelength, \simeq 13.4 ps pulse duration, and 500 MHz repetition rate) and then filtered by a Gaussian-shaped optical band-pass filter (Finisar) with tunable bandwidth, as shown in Fig. 3(a). Figure 3(b) shows the output setup for unheralded second-order correlation function ($g_u^{(2)}(\Delta t)$) measurement. Two stages of demultiplexers (each with a 200 GHz bandwidth and $>$ 85 dB adjacent channel isolation) are used exclusively for pump rejection, without additional off-chip filters. When the device is used to generate photons with high spectral purity, a significant application is as a heralded single-photon source (SPS) [31–33]. Therefore, to evaluate its performance, measurements for photon-number purity (determined by the conditioned second-order correlation function $g_h^{(2)}(\Delta t)$) and brightness are added to the output setup, as sketched in Figs. 3(c) and 3(d), respectively.

Besides, the stimulated emission tomography (SET) technique is used to reconstruct the joint spectral intensity (JSI) [42, 43]. Another relatively weak seed beam, generated by a continuous-wave (CW) laser with constant output power, is combined with the pulsed pump beam using a 90:10 beam combiner (where 90% for

pump and 10% for seed to mitigate parasitic nonlinear effects), as shown in Fig. 3(e). To reconstruct the signal-idler JSI profiles, the idler spectra corresponding to different signal (seed) wavelengths are combined to form a joint spectrum in $\{\Delta\lambda_s, \Delta\lambda_i\}$ space, where $\Delta\lambda_s$ and $\Delta\lambda_i$ represent detunings between the carrier and its neighboring resonant wavelengths.

5 Separable state generation

In the regime of separable state generation, the pump operates at a central wavelength of 1552.61 nm (channel 31 of the C-band ITU grid), while the signal and idler have central wavelengths of 1546.70 nm and 1558.52 nm, respectively. We measure the time-integrated $g_u^{(2)}(\Delta t)$ of idler photons at various pump spectral FWHM. In the low squeezing regime, the spectral purity P correlates with the zero-delay second-order correlation function $g_u^{(2)}(0)$, as described by $P = g_u^{(2)}(0) - 1$ [44, 45]. Figure 4(b) shows the measured $g_u^{(2)}(\Delta t)$ with the pump's FWHM set to 226 pm. The measured $g_u^{(2)}(0)$ is 1.955 ± 0.012 , corresponding to a spectral purity of $95.5 \pm 1.2\%$, which approximates the 97% upper limit predicted for a MRR-based SPS with only pump splitting [34]. This purity surpasses the theoretical $\sim 93\%$ upper limit of an MRR-based SPS [33, 46] without additional purity-enhancement designs. The measured JSI from the SET experiment is shown in Fig. 4(c) with the same 226 pm FWHM pump input. In the context of discrete-variable description [19], the entanglement between signal and idler photons is extracted by the Schmidt decomposition of the JSA function. Assuming a flat-phase JSA [31, 47], the Schmidt decomposition of the square root of the measured JSI yields a spectral purity of 97.2%. Although the low spectral resolution (0.02 nm) of the OSA affects the distribution of JSI, causing noticeable broadening along the $\Delta\lambda_i$ axis, the purity value remains reasonably consistent with the $g_u^{(2)}(\Delta t)$ measurements. We are more concerned with the reason for the spectral purity exceeding 93% in the presence of pump resonance splitting. Figure 4(f) shows the numerical simulation results for the JSI and its ADP function. Pump resonance splitting significantly broadens the ADP function (inset) compared to the case without pump splitting (inset of Fig. 6(e)). This broadening of the ADP function leads to a corresponding broadening of the JSI distribution along the antidiagonal direction, thereby improving spectral purity. When the pump FWHM is gradually reduced from 226 pm, the purity measured by the $g_u^{(2)}(\Delta t)$ experiment exhibits an overall decreasing trend, as shown in Fig. 4(a). We also measure several corresponding JSIs and compare them

to numerical simulations as the FWHM decreases, as shown in Appendix C.

To demonstrate the device's capability as a heralded SPS, we measure both its photon-pair generation rate and photon-number purity. In Fig. 4(d), the data points marked by the green star represent the on-chip rates when the average power at the bus's input port is set to the same value as in the previously discussed $g_u^{(2)}(\Delta t)$ experiment. After removing losses from the output grating coupler, two DEMUXs, and SNSPDs (provided in Appendix C), the estimated on-chip photon pair generation rate at this average power is 236.2 ± 0.5 kHz. The coincidence-to-accidental ratio (CAR) is 62.8 ± 0.2 , as shown in the inset of Fig. 4(d). At the same average power, the $g_h^{(2)}(0)$ value is 0.0055 ± 0.0006 , as shown in Fig. 4(e), demonstrating excellent photon-number purity for our device as a heralded SPS [45].

6 Entangled state generation

In the previous regime, the TDSI function exhibits a single-peak characteristic, as shown in Fig. 5 (a), ensuring state separability. In contrast, to generate biphoton entangled states, the TDSI function needs to be adjusted. We set the pump's central wavelength to 1546.70 nm, which aligns with the central wavelength of the unsplit R2. The relatively split R1 and R3 are chosen as the signal and idler resonances, respectively, resulting in a four-peaked TDSI function, as shown in Fig. 5 (b). Besides, the pump's FWHM is reduced to 100 pm to enhance the spectral anti-correlation between photon pairs.

Figure 6(a) shows the JSI measured using the SET technique with the Gaussian-shaped pump, which exhibits a spectral distribution with two peaks along the main diagonal direction. The corresponding simulated JSI is shown in Fig. 6(e). The other two peaks of the TDSI function along the antidiagonal direction are absent in both the measured and simulated JSI. This absence is attributed to the tight energy conservation constraints along the antidiagonal direction, caused by the unsplit pump resonance and the narrow bandwidth of the input pump pulse. This constraint is consistent with the narrow bandwidth of the simulated ADP function, as shown in the inset of Fig. 6(e).

To further engineer the spectral distribution along the antidiagonal direction, the heater voltage is set to 5.1 volts, causing the pump resonance of the PPG-MRR to spectrally overlap with the adjacent resonance of the D-MRR, as shown in Fig. 6(c). As a result, the pump is filtered with the D-MRR's transfer function (see Eq. C1 in Appendix C), which approximates an ideal differentiator's transfer function within

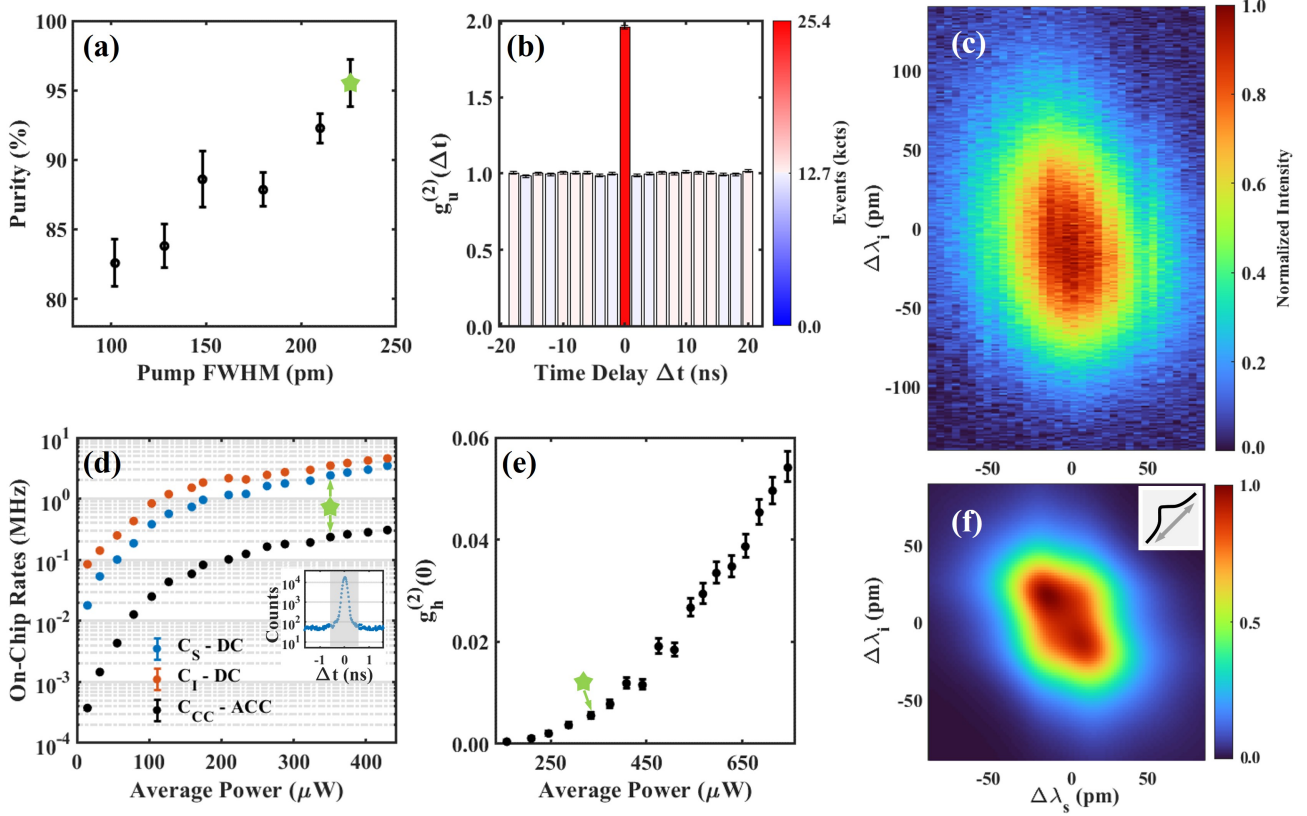


Figure 4: (a) Measured purity as a function of the spectral FWHM of the input pump pulses. Each data point corresponds to an unheralded $g_u^{(2)}(\Delta t)$ measurement. (b) Measured unheralded $g_u^{(2)}(\Delta t)$ histograms with delay for the starred data point in (a). Each histogram corresponds to a 660 ps coincidence window (33 bins, each with a 20 ps bin width). (c) Measured joint spectral intensity for the starred data point in (a), consisting of data points in a 36 ($\Delta\lambda_s$ -axis) by 282 ($\Delta\lambda_i$ -axis) grid. (d) Measured on-chip rates for signal, idler, and signal-idler coincidence as functions of input average power. The dark count rates (DC) and accidental coincidence rates (ACC) have been removed. Inset: raw coincidence counts N_{si} as a function of time delay at the average power corresponding to the green star with a 120 s integration time. The shaded area indicates a 940 ps coincidence window for the C_{CC} calculation. (e) Measured heralded $g_h^{(2)}(0)$ as a function of input average power. Error bars in (a), (b), (d), and (e) represent 1 standard deviation under Poissonian statistics. (f) Modulus squared of the simulated JSA corresponding to (c). Inset: sketch of its ADP function. The same wavelength scales are adopted in (c) and (f).

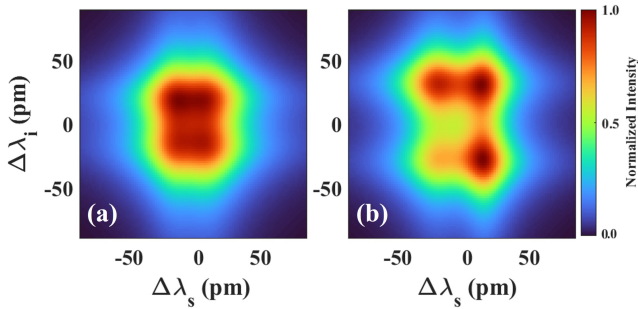


Figure 5: Simulated TDSI functions for the separable state generation regime (a) and the entangled state generation regime (b).

a narrow frequency range centered on the resonant frequency [41]. The differentiated pump pulses are then coupled into the PPG-MRR, generating photon pairs via SFWM. Figure 6(d) shows the output pulse after passing through two MRRs, monitored by a wide-bandwidth oscilloscope, which approximates 1.7-order mathematical differentiation of the input pulse (inset). Figure 6(b) shows the measured JSI for photon pairs generated by the differentiated pump. The discontinuity along the $\Delta\lambda_s$ axis is caused by the instantaneous decrease in the thermo-optic redshift of all resonances when the sweeping seed wavelength crosses the resonant wavelength of R1 [48]. The simulation results shown in Fig. 6(f) exclude the discontinuity caused by the therm-optic dispersion effect from the SET experiment, resulting in a clearer four-peaked JSI function and demonstrating wavefunction engineering along the antidiagonal direction. While maintaining the two-peaked feature along the main diagonal, the pump differentiation alters the ADP function, which is the weighted sum of two auto-convolutions contributed by the forward and backward propagating modes, respectively, as shown in Fig. 6(g) and Eq. (6). The ADP function (dashed-gray curve) exhibits a three-peaked feature in agreement with the simulated JSI's antidiagonal distribution.

7 Discussion and Conclusion

While the current device has limitations in generating a broad range of biphoton states, there is considerable potential for refinement in its programmability. By leveraging existing engineering methods, coupled resonator systems could be introduced to enable controllable resonance splitting [49, 50], and arbitrary waveform generators based on finite impulse response filters [26] or the Taylor synthesis method [27] could be employed for pump pulse shaping. These enhancements, which are fully compatible with the SOI plat-

form, could substantially improve the source's programmability. Besides, we note that the biphoton states presented in Figs. 6(a) and 6(e), following Schmidt decomposition, exhibit weights of approximately 0.91 and 0.09 for the first two Schmidt modes, respectively. This demonstrates the device's capability to generate two-dimensional entangled states for pulsed temporal-mode (PTM) encoding [16]. We believe that with the introduction of highly programmable photonic devices, this method has the potential to facilitate the controlled on-chip generation of high-dimensional entangled states for PTM encoding.

In conclusion, we have demonstrated a cavity-enhanced photon-pair source on the SOI platform that can generate both separable states with $95.5 \pm 1.2\%$ spectral purity and entangled states with two- or four-peaked biphoton spectral wavefunction in $\{\Delta\lambda_s, \Delta\lambda_i\}$ space. By choosing different resonance combinations and employing on-chip optical field differentiation, these states are engineered directly at the generation stage. A semi-analytical model is derived to simulate the biphoton spectral wavefunction in the presence of resonance splitting and pump differentiation. The model's parameters can be fully determined through measurement and fitting-based parameter extraction of the MRR's linear response. To quantify the wavefunction engineering process, we introduce two functions: TDSI and ADP. Control over these functions is consistent with our two independent adjustment methods, as demonstrated by both experiments and simulations.

Operating within the frequency-time d.o.f., the device maintains spatial single-mode properties while offering higher integration compared to PDC-based schemes and higher brightness compared to post-manipulation schemes. Through theoretical analysis and experimental validation, we have demonstrated the capability to manipulate the frequency-domain wavefunction of SFWM photon pairs on the SOI platform. The device, along with the state engineering method, holds promise for applications in long-distance quantum key distribution due to the insensitivity to polarization-mode dispersion [51–53], as well as quantum information processing based on PTM encoding [16, 17].

ACKNOWLEDGMENT

This work was supported by the National Key Research and Development Program of China (Grants No. 2021YFB2800201), the National Natural Science Foundation of China (Grants No. U22A2082), and the Ningbo Science and Technology Program (Grants No. 2023Z073).

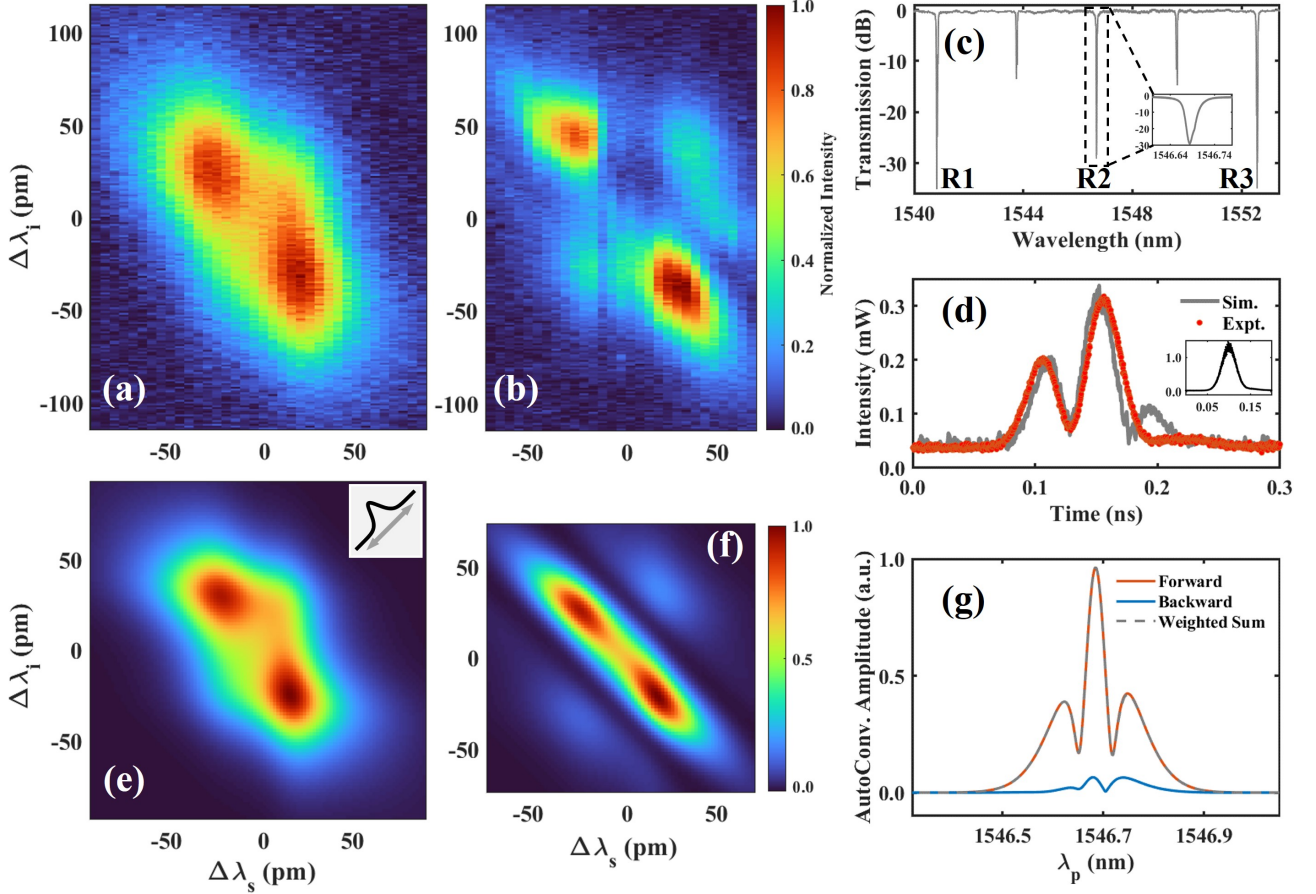


Figure 6: (a) Measured JSI with only the TDSI function engineered, consisting of data points in a 37 by 230 grid. (b) Measured JSI with both the TDSI and ADP functions engineered, consisting of data points in a 30 by 230 grid. (c) Measured spectrum with a 5.1-volt heater voltage applied to the D-MRR. (d) Waveforms of the output pump by simulation and experiment. Inset: waveform of the input pump. The oscilloscope's sample frequency is set to 40 GHz, and the averaging time is 64 for the measured waveforms. (e) Modulus squared of the simulated JSA corresponding to (a). Inset: sketch of its ADP function. (f) Modulus squared of the simulated JSA corresponding to (b). The same wavelength scales are adopted in (a), (b), (e), and (f). (g) Simulated autoconvolutions of $\alpha_p(\omega_p)l_{pf}(\omega_p)$ (forward) and $\alpha_p(\omega_p)l_{pb}(\omega_p)$ (backward), and the ADP function (weighted sum) for the JSI in (f).

AUTHOR DECLARATIONS

Conflict of Interest

The authors have no conflicts to disclose.

DATA AVAILABILITY

The data that support the findings of this study are available from the corresponding authors upon reasonable request.

APPENDIX A: LINEAR APPROXIMATION FOR PHASE MATCHING FUNCTION

The phase matching function is given by [35]

$$\begin{aligned} \phi_{PM}(\omega_p, \omega_s, \omega_i) = & \text{sinc} \left[\frac{L}{2} \Delta k(\omega_p, \omega_s, \omega_i) \right] \\ & \times \exp \left[i \frac{L}{2} \Delta k(\omega_p, \omega_s, \omega_i) \right], \end{aligned} \quad (\text{A1})$$

where L is the length of the waveguide. The phase mismatch factor $\Delta k(\omega_p, \omega_s, \omega_i)$ can be defined as

$$\begin{aligned} \Delta k(\omega_p, \omega_s, \omega_i) = & k(\omega_p) + k(\omega_s + \omega_i - \omega_p) \\ & - k(\omega_s) - k(\omega_i) - \gamma P, \end{aligned} \quad (\text{A2})$$

where γ represents the nonlinear parameter including both self-phase and cross-phase modulation, and P is the peak power of the incident pulsed pump. $k(\omega_p)$, $k(\omega_s + \omega_i - \omega_p)$, $k(\omega_s)$, and $k(\omega_i)$ are wavevectors of four interacting fields, which are expanded in first-order Taylor series at perfectly phase-matched frequencies ω_x^0 (where $x = p, s, i$ for the degenerate pump regime). The coefficients for the expansion are expressed as $k_x^{(n)}(\omega) = d^n k_x / d\omega^n |_{\omega=\omega_x^0}$. Therefore, the term $\Delta k^{(0)} \approx 2k^{(0)}(\omega_p^0) - k^{(0)}(\omega_s^0) - k^{(0)}(\omega_i^0) - \gamma P_0$ vanishes at the given P_0 , and the linear approximation for Eq. (A2) is derived as [32, 35]

$$\Delta k_{lin} = \tau_s v_s + \tau_i v_i, \quad (\text{A3})$$

where $v_s = \omega_s - \omega_s^0$ and $v_i = \omega_i - \omega_i^0$ are angular-frequency detunings. $\tau_s = k_p^{(1)}(\omega_p^0) - k_s^{(1)}(\omega_s^0)$ and $\tau_i = k_p^{(1)}(\omega_p^0) - k_i^{(1)}(\omega_i^0)$ are group-velocity mismatches.

Figure 7(a) shows the simulated $k^{(1)}$ for the fundamental TE mode of a Si waveguide with a $450\text{nm} \times 220\text{nm}$ cross-section, obtained from Ansys Lumerical MODE's dispersion calculations. The phase-matching orientation angle $\theta_{si} = -\arctan(\tau_s/\tau_i)$ is defined as the angle between the brightest strip and the λ_s -axis for

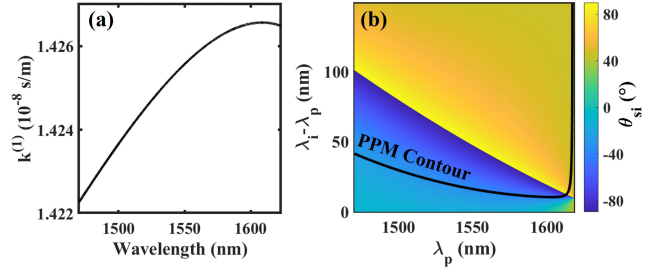


Figure 7: (a) Simulated first-order Taylor expansion coefficient in wavelength. (b) Simulated phase-matching orientation angle in $\{\lambda_p, \lambda_i - \lambda_p\}$ space. The black curve indicates the perfect phase-matching contour.

ϕ_{PM} in $\{\lambda_s, \lambda_i\}$ space, illustrating the spectral correlation of ϕ_{PM} [35, 54]. Figure 7(b) shows θ_{si} for λ_p covering S-, C-, and L-band in $\{\lambda_p, \lambda_i - \lambda_p\}$ space. The θ_{si}^0 at the perfect phase-matching (PPM) contour ranges from -33.5° to -36.3° with λ_p from 1540 nm to 1560 nm, covering the wavelength range of the experiments. These θ_{si}^0 values approximate the -45° pump envelope angle under the energy conservation constraint. This demonstrates the inevitable spectral anti-correlation of biphoton states generated in such a waveguide without MRR-enhancement or post-manipulation.

APPENDIX B: TEMPORAL COUPLED-MODE THEORY FOR MICRO-RING RESONATORS WITH RESONANCE SPLITTING

The backscattering of a MRR is caused by both the ring waveguide's sidewall roughness and the coupler's abrupt effective index transition [40]. Given these backscatterings, the optical field a , which is normalized to the optical energy stored in an all-pass MRR based on TCMT, splits into two modes: forward propagating mode a_f and backward propagating mode a_b . These two split modes of resonance with a central frequency of ω_0 satisfy

$$\frac{da_f}{dt} = i\omega_0 a_f - \frac{1}{\tau} a_f - i\mu_{12} a_b - i\kappa S_i, \quad (\text{B1a})$$

$$\frac{da_b}{dt} = i\omega_0 a_b - \frac{1}{\tau} a_b - i\mu_{21} a_f - i\kappa' S_i, \quad (\text{B1b})$$

where S_i is the amplitude of the input field. κ and κ' are the forward and backward field coupling coefficients of the coupler, respectively. μ_{12} and μ_{21} are the complex power coupling coefficients between forward and backward propagating modes within the ring waveguide. They have the same amplitude but different phases. By defining $l_j(\omega) = a_j(\omega)/S_i(\omega)$ (where

Table 1: The parameters of the four resonances located within the wavelength range of 1540 nm to 1560 nm of the PPG-MRR.

Resonance	C	$1/\tau$ (THz)	γ	μ_0 (THz)	κ ($\sqrt{\text{THz}}$)	ϕ_1	ϕ_2	ω_0 (THz)	R-squared
R1	0.920	0.0167	0.389	0.0152	0.145	1.990	4.614	1222.47	0.999
R2	0.930	0.0183	0.291	0.0114	0.159	0.793	5.262	1217.85	0.998
R3	0.976	0.0190	0.572	0.0245	0.167	1.461	4.842	1213.23	0.999
R4	0.982	0.0200	0.382	0.0161	0.164	1.740	4.688	1208.61	0.999

$j = f, b$) and solving for them in Eqs. (B1a) and (B1b), Eqs. (3) and (4) can be derived. Besides, the output field S_o at the through port is expressed as

$$S_o = S_i - i\kappa a_f - i\kappa' a_b. \quad (\text{B2})$$

To better fit the measured transmission spectra at the through port, a dimensionless factor $\gamma = \kappa'/\kappa$ is introduced. The complex μ_{12} and μ_{21} are replaced by real μ_0 , ϕ_1 , and ϕ_2 , with $\mu_{12} = \mu_0 \exp(i\phi_1)$ and $\mu_{21} = \mu_0 \exp(i\phi_2)$. The ratio of output to input fields is expressed as

$$\frac{S_o}{S_i} = C + \kappa^2 \frac{i\gamma\mu_0 (e^{i\phi_1} + e^{i\phi_2}) - (1 + \gamma^2) [i(\omega - \omega_0) + 1/\tau]}{[i(\omega - \omega_0) + 1/\tau]^2 + \mu_0^2 \exp[i(\phi_1 + \phi_2)]}, \quad (\text{B3})$$

where C is a normalized amplitude factor for compensating energy losses that may occur while measuring the spectra. Table 1 shows the free parameters in Eq. (B3) obtained by least-squares fit for the four resonances mentioned in the text, as well as R-squared values, supported by MATLAB's Curve Fitting Toolbox. The high R-squared values (≥ 0.998) demonstrate excellent agreement between the fitted curve using Eq. (B3) and the square root of the measured spectra. The fitting method always yields both forward and backward propagating modes for resonances with varying degrees of resonance splitting. For resonance R2 without significant splitting, as shown in Fig. 2(c), a "virtual" backward propagating mode can still be obtained through fitting. Consequently, our simulation is unaffected by varying degrees of resonance splitting and remains consistent across various scenarios, including the generation of separable states and entangled states.

APPENDIX C: METHODS

Purity Measurement

Figure 8 shows the measured spectra of pulses generated by the pulsed laser and filtered by the OBPF with various bandwidths. For the $g_u^{(2)}(\Delta t)$ experiment in the

separable state generation regime, the FWHM of the input pump pulses is set to 102, 128, 148, 180, 210, and 226 pm, respectively. The pulse with a 100 pm FWHM is set for the entangled state generation with the central wavelength shifted to 1552.61 nm. Spectral shapes are set to Gaussian-like for all experiments. The measured JSI with pump FWHM of 148 pm and 210 pm are shown in Figs. 8(b) and 8(c), respectively, with purity of 91.5% and 93.9% under the flat-phase assumption. The associated simulations yield purity values of 93.6% and 94.6%, obtained from the simulated results shown in Figs. 8(d) and 8(f) under the flat-phase assumption. Because of pump resonance splitting, the bandwidth of the ADP functions (shown in the insets) does not change significantly as the pump's FWHM decreases from 226 pm to 148 pm. As a result, the purity of the generated single photons experiences a minor decrease.

Brightness Measurement

The coupling loss for grating couplers (α_{gc}) is 7.0 ± 0.2 dB per facet, while the insertion loss for DEMUXs (α_{de}) is 1.9 ± 0.1 dB per stage. For signal/idler photons, the total single-channel loss (α_{tot}) from the bus waveguide output to the input of the SNSPD can be expressed as $\alpha_{tot} = 1 - 10^{(-\alpha_{gc} - 2\alpha_{de})/10}$ (in percentage), neglecting losses from all fiber connections. The average detection efficiency (η_d) of the SNSPD (Photec) is 90%. The on-chip signal/idler counts (C_X , where $X = S, I$) and the on-chip coincidence counts (C_{CC}) can be expressed using the formulas $C_X = C_{X-raw}/\eta_d/(1 - \alpha_{tot})$ and $C_{CC} = C_{CC-raw}/\eta_d^2/(1 - \alpha_{tot})^2$. Here, C_{X-raw} and C_{CC-raw} represent the raw single-channel and coincidence counts recorded by TDC, respectively. Besides, the DC and the ACC are estimated using the same method as the C_X and C_{CC} , respectively.

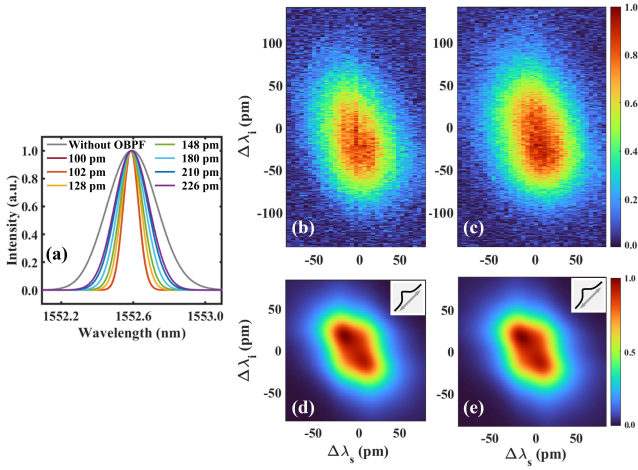


Figure 8: (a) Measured spectra for pump pulses with various spectral FWHM and for the pulse without the OBP filtering. (b)-(c) Measured JSIs with pump pulses of 210 pm (b) and 148 pm (c) FWHM, both consisting of data points in a 36 by 282 grid. (d) Modulus squared of the simulated JSA corresponding to (b). Inset: sketch of its ADP function. (e) Modulus squared of the simulated JSA corresponding to (c). Inset: sketch of its ADP function.

MRR-based Photonic Differentiator

The transfer function of an all-pass MRR is expressed as

$$H(\omega) = \frac{\tau_c - \alpha_{rt} \exp[-j\omega T_s]}{1 - \tau_c \alpha_{rt} \exp[-j\omega T_s]}, \quad (C1)$$

where τ_c is the self-coupling coefficient of the coupling region, α_{rt} is the round-trip loss coefficient, and T_s is the round-trip time delay. A Nth-order optical temporal DIFF with the transfer function $H(\omega) = [i(\omega - \omega_0)]^N$ approximates the MRR transfer function within a limited frequency range centered on the resonant frequency [41]. The order N is determined by the MRR coupling condition.

References

- [1] Jueming Bao, Zhaorong Fu, Tanumoy Pramanik, Jun Mao, Yulin Chi, Yingkang Cao, Chonghao Zhai, Yifei Mao, Tianxiang Dai, Xiaojiang Chen, et al. Very-large-scale integrated quantum graph photonics. *Nature Photonics*, pages 1–9, 2023.
- [2] Yun Zheng, Chonghao Zhai, Dajian Liu, Jun Mao, Xiaojiang Chen, Tianxiang Dai, Jieshan Huang, Jueming Bao, Zhaorong Fu, Yeyu Tong, et al. Multichip multidimensional quantum networks with entanglement retrievability. *Science*, 381(6654):221–226, 2023.
- [3] Yulin Chi, Jieshan Huang, Zhanchuan Zhang, Jun Mao, Zinan Zhou, Xiaojiang Chen, Chonghao Zhai, Jueming Bao, Tianxiang Dai, Huihong Yuan, et al. A programmable qudit-based quantum processor. *Nature communications*, 13(1):1166, 2022.
- [4] Christian Reimer, Michael Kues, Piotr Roztocki, Benjamin Wetzell, Fabio Grazioso, Brent E Little, Sai T Chu, Tudor Johnston, Yaron Bromberg, Lucia Caspani, et al. Generation of multiphoton entangled quantum states by means of integrated frequency combs. *Science*, 351(6278):1176–1180, 2016.
- [5] Daniel Llewellyn, Yunhong Ding, Imad I Faruque, Stefano Paesani, Davide Bacco, Raffaele Santagati, Yan-Jun Qian, Yan Li, Yun-Feng Xiao, Marcus Huber, et al. Chip-to-chip quantum teleportation and multi-photon entanglement in silicon. *Nature Physics*, 16(2):148–153, 2020.
- [6] Liangliang Lu, Lijun Xia, Zhiyu Chen, Leizhen Chen, Tonghua Yu, Tao Tao, Wenchao Ma, Ying Pan, Xinlun Cai, Yanqing Lu, et al. Three-dimensional entanglement on a silicon chip. *npj Quantum Information*, 6(1):30, 2020.
- [7] Poolad Imany, Jose A Jaramillo-Villegas, Ogaga D Odele, Kyunghun Han, Daniel E Leaird, Joseph M Lukens, Pavel Lougovski, Minghao Qi, and Andrew M Weiner. 50-ghz-spaced comb of high-dimensional frequency-bin entangled photons from an on-chip silicon nitride microresonator. *Optics express*, 26(2):1825–1840, 2018.
- [8] Marco Clementi, Federico Andrea Sabattoli, Massimo Borghi, Linda Gianini, Noemi Tagliavacche, Houssein El Dirani, Laurene Youssef, Nicola Bergamasco, Camille Petit-Etienne, Erwine Pargon, et al. Programmable frequency-bin quantum states in a nano-engineered silicon device. *Nature Communications*, 14(1):176, 2023.
- [9] Massimo Borghi, Noemi Tagliavacche, Federico Andrea Sabattoli, Houssein El Dirani, Laurene Youssef, Camille Petit-Etienne, Erwine Pargon, JE Sipe, Marco Liscidini, Corrado Sciancalepore, et al. Reconfigurable silicon photonic chip for the generation of frequency-bin-entangled qudits. *Physical Review Applied*, 19(6):064026, 2023.
- [10] Jieshan Huang, Xudong Li, Xiaojiang Chen, Chonghao Zhai, Yun Zheng, Yulin Chi, Yan Li, Qiongyi He, Qihuang Gong, and Jianwei Wang.

- Demonstration of hypergraph-state quantum information processing. *Nature Communications*, 15(1):2601, 2024.
- [11] Nicolas J Cerf, Mohamed Bourennane, Anders Karlsson, and Nicolas Gisin. Security of quantum key distribution using d-level systems. *Physical review letters*, 88(12):127902, 2002.
- [12] Julio T Barreiro, Tzu-Chieh Wei, and Paul G Kwiat. Beating the channel capacity limit for linear photonic superdense coding. *Nature physics*, 4(4):282–286, 2008.
- [13] Ranjeet Kumar, Jun Rong Ong, Marc Savanier, and Shayan Mookherjea. Controlling the spectrum of photons generated on a silicon nanophotonic chip. *Nature communications*, 5(1):5489, 2014.
- [14] C Xiong, X Zhang, A Mahendra, J He, D-Y Choi, CJ Chae, D Marpaung, Arne Leinse, RG Heide- man, M Hoekman, et al. Compact and reconfigurable silicon nitride time-bin entanglement circuit. *Optica*, 2(8):724–727, 2015.
- [15] Lan-Tian Feng, Ming Zhang, Xiao Xiong, Di Liu, Yu-Jie Cheng, Fang-Ming Jing, Xiao-Zhuo Qi, Yang Chen, De-Yong He, Guo-Ping Guo, et al. Transverse mode-encoded quantum gate on a silicon photonic chip. *Physical Review Letters*, 128(6):060501, 2022.
- [16] Vahid Ansari, John M. Donohue, Benjamin Brecht, and Christine Silberhorn. Tailoring non-linear processes for quantum optics with pulsed temporal-mode encodings. *Optica*, 5(5):534–550, May 2018.
- [17] Benjamin Brecht, Dileep V Reddy, Christine Silberhorn, and Michael G Raymer. Photon temporal modes: a complete framework for quantum information science. *Physical Review X*, 5(4):041017, 2015.
- [18] Andreas Eckstein, Andreas Christ, Peter J Mosley, and Christine Silberhorn. Highly efficient single-pass source of pulsed single-mode twin beams of light. *Physical Review Letters*, 106(1):013603, 2011.
- [19] Benjamin Brecht and Christine Silberhorn. Characterizing entanglement in pulsed parametric down-conversion using chronocyclic wigner functions. *Physical Review A*, 87(5):053810, 2013.
- [20] Guillaume Boucher, Tom Douce, David Bresteau, Stephen P Walborn, Arne Keller, Thomas Coudreau, Sara Ducci, and Perola Milman. Tool- box for continuous-variable entanglement production and measurement using spontaneous parametric down-conversion. *Physical Review A*, 92(2):023804, 2015.
- [21] Saverio Francesconi, Florent Baboux, Arnault Raymond, Nelly Fabre, Guillaume Boucher, Aristide Lemaitre, Perola Milman, Maria Ines Amanti, and Sara Ducci. Engineering two-photon wavefunction and exchange statistics in a semi-conductor chip. *Optica*, 7(4):316–322, 2020.
- [22] Vahid Ansari, John M Donohue, Markus All- gaier, Linda Sansoni, Benjamin Brecht, Jonathan Roslund, Nicolas Treps, Georg Harder, and Christine Silberhorn. Tomography and purification of the temporal-mode structure of quantum light. *Physical review letters*, 120(21):213601, 2018.
- [23] Vahid Ansari, Emanuele Roccia, Matteo Santan- drea, Mahnaz Doostdar, Christof Eigner, Laura Padberg, Ilaria Gianani, Marco Sbroscia, John M Donohue, Luca Mancino, et al. Heralded generation of high-purity ultrashort single photons in programmable temporal shapes. *Optics express*, 26(3):2764–2774, 2018.
- [24] Rui-Bo Jin, Kurumi Tazawa, Naoto Asamura, Masahiro Yabuno, Shigehito Miki, Fumihiro China, Hirotaka Terai, Kaoru Minoshima, and Ryosuke Shimizu. Quantum optical synthesis in 2d time–frequency space. *APL Photonics*, 6(8), 2021.
- [25] Rui-Bo Jin, Hiroki Oshima, Takumi Yagisawa, Masahiro Yabuno, Shigehito Miki, Fumihiro China, Hirotaka Terai, and Ryosuke Shimizu. Two-photon spectral modulation via temporal manipulation: Quantum optical synthesis of spectral modes from temporal square waves. *Applied Physics Letters*, 121(24), 2022.
- [26] Shasha Liao, Yunhong Ding, Jianji Dong, Ting Yang, Xiaolin Chen, Dingshan Gao, and Xin- liang Zhang. Arbitrary waveform generator and differentiator employing an integrated optical pulse shaper. *Optics express*, 23(9):12161–12173, 2015.
- [27] Shasha Liao, Yunhong Ding, Jianji Dong, Siqi Yan, Xu Wang, and Xinliang Zhang. Photonic arbitrary waveform generator based on taylor syn-

- thesis method. *Optics Express*, 24(21):24390–24400, 2016.
- [28] Weilin Liu, Ming Li, Robert S Guzzon, Erik J Norberg, John S Parker, Mingzhi Lu, Larry A Coldren, and Jianping Yao. A fully reconfigurable photonic integrated signal processor. *Nature Photonics*, 10(3):190–195, 2016.
- [29] MB Danailov and IP Christov. Time-space shaping of light pulses by fourier optical processing. *Journal of modern optics*, 36(6):725–731, 1989.
- [30] Joshua W Silverstone, Damien Bonneau, Kazuya Ohira, Nob Suzuki, Haruhiko Yoshida, Norio Iizuka, Mizunori Ezaki, Chandra M Natarajan, Michael G Tanner, Robert H Hadfield, et al. On-chip quantum interference between silicon photon-pair sources. *Nature Photonics*, 8(2):104–108, 2014.
- [31] Ben M. Burrige, Imad I. Faruque, John G. Rarity, and Jorge Barreto. Integrate and scale: a source of spectrally separable photon pairs. *Optica*, 10(11):1471–1477, Nov 2023.
- [32] Stefano Paesani, Massimo Borghi, Stefano Signorini, Alexandre Maïnos, Lorenzo Pavesi, and Anthony Laing. Near-ideal spontaneous photon sources in silicon quantum photonics. *Nature communications*, 11(1):2505, 2020.
- [33] Yingwen Liu, Chao Wu, Xiaowen Gu, Yuechan Kong, Xinxin Yu, Renyou Ge, Xinlun Cai, Xiaogang Qiang, Junjie Wu, Xuejun Yang, et al. High-spectral-purity photon generation from a dual-interferometer-coupled silicon microring. *Optics Letters*, 45(1):73–76, 2020.
- [34] Will McCutcheon. Backscattering in nonlinear microring resonators via a gaussian treatment of coupled cavity modes. *APL Photonics*, 6(6), 2021.
- [35] K Garay-Palmett, HJ McGuinness, Offir Cohen, JS Lundeen, R Rangel-Rojo, AB U’ren, MG Raymer, CJ McKinstrie, S Radic, and IA Walmsley. Photon pair-state preparation with tailored spectral properties by spontaneous four-wave mixing in photonic-crystal fiber. *Optics express*, 15(22):14870–14886, 2007.
- [36] Z Vernon, M Menotti, CC Tison, JA Steidle, ML Fanto, PM Thomas, SF Preble, AM Smith, PM Alsing, M Liscidini, et al. Truly unentangled photon pairs without spectral filtering. *Optics letters*, 42(18):3638–3641, 2017.
- [37] Jesper Bjerger Christensen, Jacob Gade Koefoed, Karsten Rottwitt, and CJ McKinstrie. Engineering spectrally unentangled photon pairs from nonlinear microring resonators by pump manipulation. *Optics letters*, 43(4):859–862, 2018.
- [38] Shanhui Fan, Wonjoo Suh, and John D Joannopoulos. Temporal coupled-mode theory for the fano resonance in optical resonators. *JOSA A*, 20(3):569–572, 2003.
- [39] Wim Bogaerts, Peter De Heyn, Thomas Van Vaerenbergh, Katrien De Vos, Shankar Kumar Selvaraja, Tom Claes, Pieter Dumon, Peter Bienstman, Dries Van Thourhout, and Roel Baets. Silicon microring resonators. *Laser & Photonics Reviews*, 6(1):47–73, 2012.
- [40] Ang Li, Thomas Van Vaerenbergh, Peter De Heyn, Peter Bienstman, and Wim Bogaerts. Backscattering in silicon microring resonators: a quantitative analysis. *Laser & Photonics Reviews*, 10(3):420–431, 2016.
- [41] Aoling Zheng, Jianji Dong, Linjie Zhou, Xi Xiao, Qi Yang, Xinliang Zhang, and Jianping Chen. Fractional-order photonic differentiator using an on-chip microring resonator. *Optics Letters*, 39(21):6355–6358, 2014.
- [42] Marco Liscidini and JE Sipe. Stimulated emission tomography. *Physical review letters*, 111(19):193602, 2013.
- [43] Andreas Eckstein, Guillaume Boucher, Aristide Lemaître, Pascal Filloux, Ivan Favero, Giuseppe Leo, John E Sipe, Marco Liscidini, and Sara Ducci. High-resolution spectral characterization of two photon states via classical measurements. *Laser & Photonics Reviews*, 8(5):L76–L80, 2014.
- [44] Andreas Christ, Kaisa Laiho, Andreas Eckstein, Katiúscia N Cassemiro, and Christine Silberhorn. Probing multimode squeezing with correlation functions. *New Journal of Physics*, 13(3):033027, 2011.
- [45] S Signorini and L Pavesi. On-chip heralded single photon sources. *AVS Quantum Science*, 2(4), 2020.
- [46] Lukas G Helt, Zhenshan Yang, Marco Liscidini, and John E Sipe. Spontaneous four-wave mixing in microring resonators. *Optics letters*, 35(18):3006–3008, 2010.
- [47] Ben M Burrige, Imad I Faruque, John G Rarity, and Jorge Barreto. High spectro-temporal purity

single-photons from silicon micro-racetrack resonators using a dual-pulse configuration. *Optics Letters*, 45(14):4048–4051, 2020.

- [48] Marc De Cea, Amir H Atabaki, and Rajeev J Ram. Power handling of silicon microring modulators. *Optics express*, 27(17):24274–24285, 2019.
- [49] Mian Zhang, Cheng Wang, Yaowen Hu, Amirhassan Shams-Ansari, Tianhao Ren, Shan-hui Fan, and Marko Lončar. Electronically programmable photonic molecule. *Nature Photonics*, 13(1):36–40, 2019.
- [50] Yoshitomo Okawachi, Bok Young Kim, Yun Zhao, Xingchen Ji, Michal Lipson, and Alexander L Gaeta. Dynamic control of photon lifetime for quantum random number generation. *Optica*, 8(11):1458–1461, 2021.
- [51] Qiang Zhang, Hiroki Takesue, Sae Woo Nam, Carsten Langrock, Xiuping Xie, Burm Baek, Martin M Fejer, and Yoshihisa Yamamoto. Distribution of time-energy entanglement over 100 km fiber using superconducting single-photon detectors. *Optics express*, 16(8):5776–5781, 2008.
- [52] J Nunn, LJ Wright, C Söller, L Zhang, IA Walmsley, and BJ Smith. Large-alphabet time-frequency entangled quantum key distribution by means of time-to-frequency conversion. *Optics express*, 21(13):15959–15973, 2013.
- [53] Xiaodong Shi, Kai Guo, Jesper Bjerge Christensen, Mario A Usuga Castaneda, Xuanming Liu, Haiyan Ou, and Karsten Rottwitt. Multi-channel photon-pair generation with strong and uniform spectral correlation in a silicon microring resonator. *Physical Review Applied*, 12(3):034053, 2019.
- [54] Shivani Sharma, Vivek Venkataraman, and Joyee Ghosh. Spectrally-pure integrated telecom-band photon sources in silicon. *Journal of Lightwave Technology*, 40(23):7529–7537, 2022.